Banner appropriate to article type will appear here in typeset article

# Bistability of interfacial long waves in two-layer Couette flow

## Xingyu Wang<sup>1</sup>, Demetrios T. Papageorgiou<sup>1</sup>† and Pierre Germain<sup>1</sup>

<sup>1</sup>Department of Mathematics, Imperial College London, London SW7 2AZ, UK

(Received xx; revised xx; accepted xx)

This paper investigates the stability of interfacial long waves in two-layer plane Couette flow using an asymptotic model developed in Kalogirou *et al.* (2016) to match the experimental findings of Barthelet *et al.* (1995). Concentrating on the bistable regime, we show a remarkable agreement with the asymptotic model, both qualitatively and quantitatively. The two stable traveling waves are identified and their basins of attraction characterized via different initial conditions.

#### 1. Introduction

The stability of two-fluid plane Couette–Poiseuille configurations has a long history beginning with Yih (1967), who showed that the flow is unstable to long waves at nonzero Reynolds numbers. This instability arises from the viscosity discontinuity at the interface and depends on both the viscosity and thickness ratios of the two fluid layers. Subsequent analyses established the thin-layer effect—namely that when the thin layer is also the more viscous one the flow is generically linearly unstable (Hooper & Boyd 1983; Hooper 1985; Renardy 1985, 1987). Weakly nonlinear reductions connected these results to dispersive Kuramoto-Sivashinsky-type amplitude equations and travelling wave solutions (Hooper & Grimshaw 1985, 1988; Charru & Fabre 1994), while broader reviews of multilayer film dynamics delineated the scope and limitations of lubrication approaches (Craster & Matar 2009). More recently, Mohammadi & Smits (2017) performed a comprehensive linear stability analysis of two-layer Couette flows over wide ranges of viscosity and thickness ratios, and identified a new interfacial mode at very low viscosity ratios motivated by liquidinfused and superhydrophobic surface applications. Motivated by the canonical annulardevice observations of long-wave asymmetry and, at higher drive, bistability (Barthelet et al. 1995), recent developments introduced an inertia-retaining nonlocal model for two-layer Couette flow in which the thick layer enters via the Orr-Sommerfeld problem at leading order (Kalogirou et al. 2016), enabling quantitative comparisons at experimentally relevant Reynolds numbers.

This study focuses on reproducing the cases with thickness ratio d=0.25 from the experiments of Barthelet *et al.* (1995) using model computations, namely for  $U/U_L \in \{1.06, 1.13, 1.33, 1.58, 1.77, 2.25, 2.43\}$ , with particular emphasis on the last case, which exhibits bistability in the experiment (see for example figure 22 in Barthelet *et al.* (1995)). Present computations expand the parameter sets analysed by Kalogirou *et al.* (2016): their

figure 3 treated  $U/U_L \in \{1.33, 1.58, 1.77\}$  and showed good agreement between the model, DNS, and experiment, whereas their figure 4 addressed  $U/U_L = 2.43$  ( $Re_1 \approx 709$ ) and captured coexisting k = 1 (unimodal) and k = 2 (bimodal) branches, but with less satisfactory agreement with the experiment in the bimodal case. The asymptotic formulation used in both studies builds on the nonlocal thin-film model for surfactant-laden two-fluid Couette flows derived by Kalogirou & Papageorgiou (2016), in which the evolution of the thin upper layer is coupled to the inertia-retaining motion of the thick lower layer via a leading-order Orr–Sommerfeld problem. Here we produce all possible comparisons with the experiments, quantify interfacial shapes and harmonic amplitudes, and study the basins of attraction of L-and 2L-periodic attractors in the bistability case, thereby providing a focused, quantitative account of the bistable regime within a comprehensive experiment-model comparison.

A number of closely related nonlocal long-wave models have been developed for multilayer shear and pressure-driven flows. For instance, Kalogirou et al. (2020) derived and validated an asymptotic description of multilayer Poiseuille flow that couples thin and thick layers through a nonlocal term, while Kalogirou & Blyth (2023) used a lubrication model of similar structure to study Rayleigh-Taylor-type instability in an unstably stratified two-layer shear flow. Interfacial slip has been incorporated into such models by Katsiavria & Papageorgiou (2022), who derived a nonlocal evolution equation for multilayer shear flows with Navier slip, and by Papageorgiou & Tanveer (2023), who showed that even weak interfacial slip can have a singular destabilising effect in an otherwise highly stable two-layer Couette configuration. A closely related nonlocal Couette flow model for the complementary geometry with the thin layer below (opposite to the present configuration), in the absence of slip, has been analysed in detail by Papageorgiou & Tanveer (2019), who computed large-amplitude travelling waves, and by Mora Saenz & Tanveer (2024), who gave a rigorous spectral stability theory for these waves. More generally, the mathematical properties of multi-dimensional nonlocal systems arising from thin-layer reductions have been studied in Papageorgiou & Tanveer (2021), while analogous nonlocal formulations for viscoelastic two-fluid Couette flow were derived and explored numerically in Ray et al. (2018). Recent work on the linear stability of viscous multilayer shear flows with interfacial slip (Katsiavria & Papageorgiou 2024) provides further context for the present study and underlines the broad relevance of nonlocal models of the type considered here.

The structure of the rest of this paper is as follows. In §2, we summarise the experiments of Barthelet  $et\ al.$  (1995) and fix the physical and dimensionless parameters used for comparison with the model. In §3, we present the nonlocal long-wave model for two-layer Couette flow, recalling its derivation. In §4, we carry out an in-depth study of the bistable regime, computing finite-amplitude travelling waves, analysing their stability, comparing the wave profiles with the experiment, and characterising their basins of attraction. In §5, we broaden the comparison with Barthelet et al. (1995) to all accessible cases at d=0.25, examining interfacial profiles and harmonic amplitudes across Reynolds numbers. Finally, a discussion can be found in §6.

## 2. The experiments of Barthelet et al. (1995)

The experiments of Barthelet *et al.* (1995) were performed in an annular Couette device formed by bending a long rectangular channel into a ring. The upper plate is driven at a prescribed speed U, and the interfacial amplitude is monitored at a fixed azimuthal location. The configuration consists of a thin, more viscous layer above a thicker, less viscous one, with thickness ratio  $d = h_2/h_1$  (thin-layer thickness over thick-layer thickness). For sufficiently small d (in particular d = 0.25, the smallest value examined), the experiments report a supercritical onset of travelling waves whose wavelength equals the device circumference; at

Physical parameter	Value	Physical parameter	Value
Channel mean diameter D	0.40 m	Channel width W	0.04 m
Channel height (depth) $d_{\text{phys}}$	0.02 m	Thickness ratio $d = h_2/h_1$	0.25
Lower fluid viscosity $\mu_1$	0.0108 Pas	Upper fluid viscosity $\mu_2$	0.0297 Pas
Lower fluid density $\rho_1$	$1142 \text{ kg m}^{-3}$	Upper fluid density $\rho_2$	$846 \text{ kg m}^{-3}$
Viscosity ratio $m = \mu_2/\mu_1$	2.76	Density ratio $r = \rho_2/\rho_1$	0.741
Surface tension $\gamma$	0.03 Pa m		

Table 1: Physical parameters from the experiments of Barthelet et al. (1995).

higher speeds a bistable response is observed in which unimodal (L-periodic) and bimodal (2L-periodic) waves coexist and are excited by different initial conditions (see Barthelet  $et\ al.$  (1995), pp. 48-50). Fluid properties for the commonly used pair "1d-2" at 20°C are collected in table 1. Since our model is derived under the assumption  $d \ll 1$ , other cases (d = 0.33, 0.42 and 0.82) in Barthelet  $et\ al.$  (1995) are not considered here. Although d = 0.25 is the closest case to the model's asymptotic regime, some behaviours are not captured because d is not asymptotically small. Nevertheless, most qualitative features are reproduced.

The experiments at d=0.25 identify a critical upper-plate speed above which a supercritical bifurcation produces a travelling wave with wavelength equal to the mean channel perimeter  $L_w=\pi D=1.257$  m, implying a dimensionless period  $2L=L_w/d_{\rm phys}\approx 63$ . The interfacial amplitude is recorded by a fixed probe, and spatial profiles follow from this signal if the wave speed is known—this is also how we post-process the computations. We introduce the small parameter  $\varepsilon=h_1/(h_1+h_2)=d/(1+d)\ll 1$  for the non-dimensional upper-layer thickness. The undisturbed interfacial speed is defined as in Kalogirou *et al.* (2016),  $U_s=1-\varepsilon/(m-(m-1)\varepsilon)$ . In the model we sample at x=0, where  $x:=x_{\rm lab}-U_st$  is the Galilean coordinate; a  $2\pi$ -periodic travelling wave H(x-ct) then has model period  $2\pi/c$ . To compare with experiments that probe at a fixed laboratory position  $x_{\rm lab}=0$ , this period is multiplied by  $c/U_s$ . As in Kalogirou *et al.* (2016), we scale the oscillatory part as in the experiments by defining  $S(t)=S(0,t)-(1-\varepsilon)$  and compute  $A_+=\max_t S(t)$  and  $A_-=\min_t S(t)$ . The scaled amplitude is  $S(t)/S_{\rm sat}$ , where  $S_{\rm sat}=\frac{1}{2}(A_+-A_-)$ .

In the model, we assume  $\rho_1 = \rho_2 = \rho$  (although in the experiment they differ; see table 1) and the resulting non-dimensionalised parameters are

$$Re_1 = \frac{\rho U d_{\text{phys}}}{\mu_1}, \qquad Re_2 = \frac{\rho U d_{\text{phys}}}{\mu_2}, \qquad We = \frac{\rho U^2 d_{\text{phys}}}{\gamma}, \qquad Ca = \frac{\mu_2 U}{\gamma}.$$
 (2.1)

#### 3. Mathematical model

The derivation of this model was first presented in Kalogirou *et al.* (2016). The derivation starts from the Navier–Stokes formulation for two immiscible layers in a channel, with the top wall translating at constant speed to impose shear. Assuming a thin upper film, they perform an asymptotic reduction that yields a nonlinear, nonlocal evolution equation for the interface; the corresponding flow field in the bulk of each layer follow directly from this reduced description.

Lengths are non-dimensionalised with the channel depth  $d_{phys}$ , velocity with the upperplate speed U, time with  $d_{phys}/U$  and pressures with  $\rho U^2$ , where the phase densities are taken equal. Recall the non-dimensional upper-layer thickness is defined as  $\varepsilon \ll 1$ , we place the interface at  $y = 1 - \varepsilon + \varepsilon^2 H(x,t)$  (see figure 1). To derive an evolution equation for H, the Navier-Stokes equations are solved asymptotically in the thin upper layer (long-wave scaling)

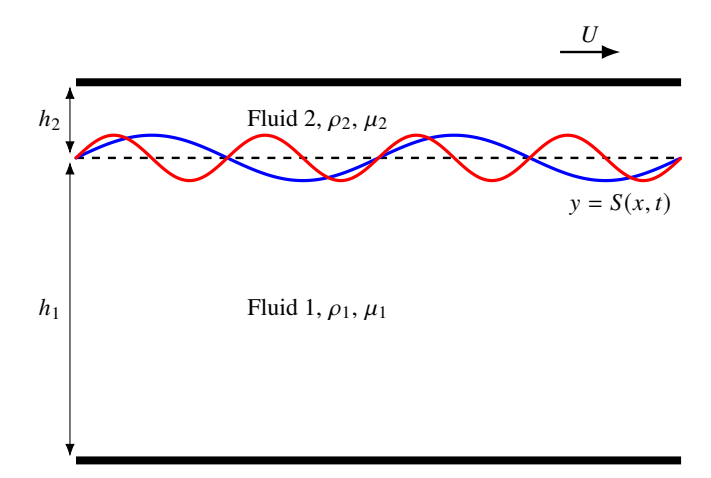


Figure 1: Two superposed fluid layers in a channel, driven by the upper-plate shear with speed U. Blue and red curves represent unimodal and bimodal respectively.  $d = h_2/h_1 = 0.25$  and  $U_L = 0.138 \,\mathrm{m \, s^{-1}}$  fixed across the cases, while  $U/U_L$  varies.

and in the thick lower layer (which supplies a nonlocal inertial response). At the interface, the kinematic condition, continuity of normal velocity and normal stress, and continuity of tangential velocities are enforced.

Transforming equation (3.12) (Kalogirou *et al.* 2016) via  $(t, x, H) \rightarrow (t/v, x/\sqrt{v}, -\sqrt{v}H)$ , with  $v = (2\pi/2L)^2 = 0.01$ , yields a  $2\pi$ -periodic problem consistent with the model used in equation (2.8) of Papageorgiou & Tanveer (2023); here we adopt the corresponding no-slip version

$$H_t + H H_x + \nu H_{xxxx} + \sum_{k \in \mathbb{Z}} N[k] \, \hat{H}_k \, e^{ikx} = 0, \tag{3.1}$$

where

$$N[k] = -i\frac{\Lambda}{2\nu} k \sqrt{\nu} F''(1;\alpha), \qquad \alpha = k \sqrt{\nu}. \tag{3.2}$$

Here  $\Lambda = 3Ca_0/2m$  with  $Ca_0 = Ca/\varepsilon = O(1)$  encodes the interlayer coupling. Note that  $\Lambda$  follows the convention of Papageorgiou & Tanveer (2023), whereas Kalogirou *et al.* (2016) absorb the factor 1 - 1/m into  $\Lambda$ . Here that factor is absorbed into the Orr–Sommerfeld boundary condition, so the formulations are equivalent. The function  $F(y;\alpha)$  is determined by a quasi-static Orr–Sommerfeld problem that captures inertial response in the thick (lower) layer,

$$\left(\frac{d^2}{dy^2} - \alpha^2\right)^2 F - i \alpha R (y - 1) \left(\frac{d^2}{dy^2} - \alpha^2\right) F = 0, \quad 0 < y < 1, \tag{3.3}$$

subject to no-slip boundary conditions,

$$F(0) = F'(0) = 0,$$
  $F(1) = 0,$   $F'(1) = \frac{m-1}{m},$  (3.4)

where  $R = Re_1$  is the Reynolds number of the thick (lower) layer.  $F''(1;\alpha)$  in (3.2) can be obtained numerically from (3.3)-(3.4), or via the closed-form representation in Papageorgiou & Tanveer (2023, §3). In the present work we take the no-slip limit (slip length l = 0).

The model parameters are R,  $\Lambda$ , m and  $\nu$ . For a given fluid pair, m,  $\nu$  are fixed, and  $R \propto U$ . Although we define earlier  $\Lambda = 3 C a_0/(2m)$ , in practice,  $Ca = \mu_2 U/\gamma$  is known from the experimental data but  $Ca_0$  is not independently measurable (it is defined only through the

canonical scaling  $Ca = \varepsilon Ca_0$ ), so for quantitative comparison at finite  $\varepsilon$  we treat  $\Lambda$  as an adjustable parameter.

### 4. In-depth study of the bistability case

In this section, we first compute travelling wave solutions of (3.1) and identify their stability. We then compare interfacial profiles with the experiment and delineate basins of attraction.

#### 4.1. Finite-amplitude travelling waves and their stability

The procedure we follow here is the same as in Papageorgiou & Tanveer (2023). We seek travelling wave solutions of (3.1) in the co-moving coordinate z = x - Ct, where C is the wave speed, writing H(x,t) = H(z). Substitution into (3.1) gives

$$-C H_z + H H_z + \nu H_{zzzz} + \sum_{k \in \mathbb{Z}} N[k] \hat{H}_k e^{ikz} = 0.$$
 (4.1)

Represent H by a truncated Fourier series  $H(z) = \sum_{k=-N}^{N} \hat{H}_k e^{ikz}$ , where  $\hat{H}_{-k} = \overline{\hat{H}_k}$  and  $\hat{H}_0 = 0$ . Using  $N[-k] = \overline{N[k]}$  and N[0] = 0, the Fourier coefficients of (4.1) satisfy

$$-ik C \hat{H}_k + \frac{ik}{2} (\hat{H} * \hat{H})(k) + \nu k^4 \hat{H}_k + N[k] \hat{H}_k = 0, k \in \mathbb{Z}^+.$$
 (4.2)

Translation invariance is removed by a phase condition. We impose

$$\Im \hat{H}_{k_0} = 0. \tag{4.3}$$

For the first branch of solutions we set  $k_0 = 1$ ; For the second branch, for which  $\hat{H}_k = 0$  for all odd k, we instead set  $k_0 = 2$ . Equations (4.2)-(4.3), define a nonlinear algebraic system for the 2N real unknowns ( $\Re \hat{H}_1$ , C,  $\Re \hat{H}_2$ ,  $\Im \hat{H}_2$ , ...,  $\Re \hat{H}_N$ ,  $\Im \hat{H}_N$ ), which we solve by Newton iteration.

For linear stability of the travelling wave solution, we perturb in Fourier space as  $\hat{H}_k(t) = \hat{H}_k + \epsilon \hat{U}_k e^{\sigma t}$  with  $\epsilon \ll 1$ , substitute into (3.1), and retain  $O(\epsilon)$  terms to obtain the eigenvalue problem

$$-(\nu k^{4} + N[k] - iCk) \hat{U}_{k} - ik (\hat{U} * \hat{H})(k) = \sigma \hat{U}_{k}, \qquad k \in \{-N, \dots, -1, 1, \dots, N\}.$$
(4.4)

This assembles into a  $2N \times 2N$  complex matrix acting on the vector of perturbation coefficients ordered as  $(\hat{U}_1, \hat{U}_{-1}, \hat{U}_2, \hat{U}_{-2}, \dots, \hat{U}_N, \hat{U}_{-N})^T$ .

Throughout § 4, we set R=709,  $\nu=0.01$ , m=2.76, following Barthelet *et al.* (1995). In figure 2, the fundamental  $2\pi$ -periodic family (branch 1) is stable just beyond onset and remains stable up to  $\Lambda\approx0.040$ . At this value the dominant eigenvalue crosses the imaginary axis with nonzero frequency, and branch 1 loses stability via a Hopf bifurcation. The evenharmonic  $\pi$ -periodic family (branch 2) emerges at  $\Lambda\approx0.010$  via a steady bifurcation from the flat state and is initially unstable; it stabilises at  $\Lambda\approx0.016$  and remains stable until  $\Lambda\approx0.035$ , after which it is unstable on [0.036, 0.057] and restabilises at  $\Lambda\approx0.057$ , and stays stable at least up to  $\Lambda\approx0.090$  before losing stability again. There is a clear bistability window  $0.016\lesssim\Lambda\lesssim0.035$  in which branches 1 and 2 are simultaneously stable.

At  $\Lambda \approx 0.0358$ , branch 2 undergoes a steady secondary bifurcation, giving rise to a new steady branch. The new branch is immediately stable (not shown in figure 2), while branch 2 loses stability at the same point. This exchange of stability is consistent with a supercritical pitchfork, as the critical eigenvalue is real at onset. The new branch stays stable until  $\Lambda = 0.1367$ , where it undergoes a Hopf bifurcation and loses stability.

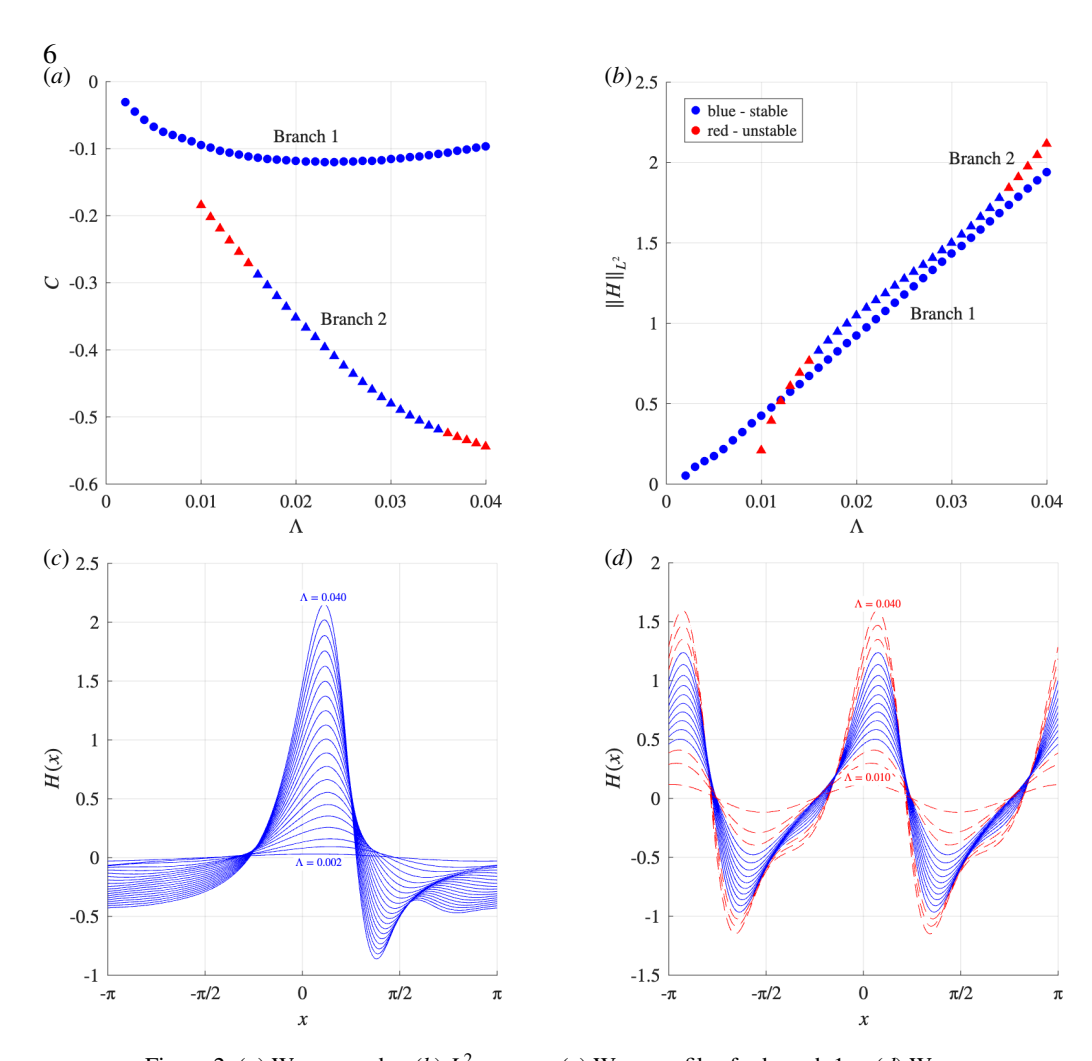


Figure 2: (a) Wave speed. (b)  $L^2$  norm. (c) Wave profiles for branch 1. (d) Wave profiles for branch 2. Parameter values: R = 709, v = 0.01, m = 2.76.

#### 4.2. *Comparison with the experiments of Barthelet* et al. (1995)

We integrate equation 3.1 using a Fourier spectral discretisation in space and a fourth-order exponential-time-differencing Runge–Kutta method in time.

The experimental taxonomy at d=0.25 reports a bistable window at the highest plate speeds in which unimodal (L-periodic) and bimodal (2L-periodic) responses coexist and are selected by initial data (Barthelet *et al.* 1995, pp. 48-50). We use two small-amplitude initial conditions that target the competing attractors:

$$H(x,0) = A\sin(x)$$
 (branch 1),  $H(x,0) = A\sin(2x)$  (branch 2),

where in practice we set  $A=10^{-3}$ . We fix  $\Lambda=0.020$  to reproduce the observed coexistence: the first seed saturates to a non-symmetric 2L-periodic wave with pronounced front-trough asymmetry, while the second remains bimodal throughout the evolution, with only even harmonics present in the probe signal. Indeed, one can choose any  $\Lambda \in [0.016, 0.035]$ , and we simply choose the  $\Lambda$  which has the closest wave profile as in the experiment.

In figure 3(b), the  $T_{\text{sat}}$  is scaled to 16/3 s for branch 1 and 8/3 s for branch 2, matching figure 3(a). From the model computation, the real  $T_{\text{sat}} = 4.039$  s for branch 1. The model

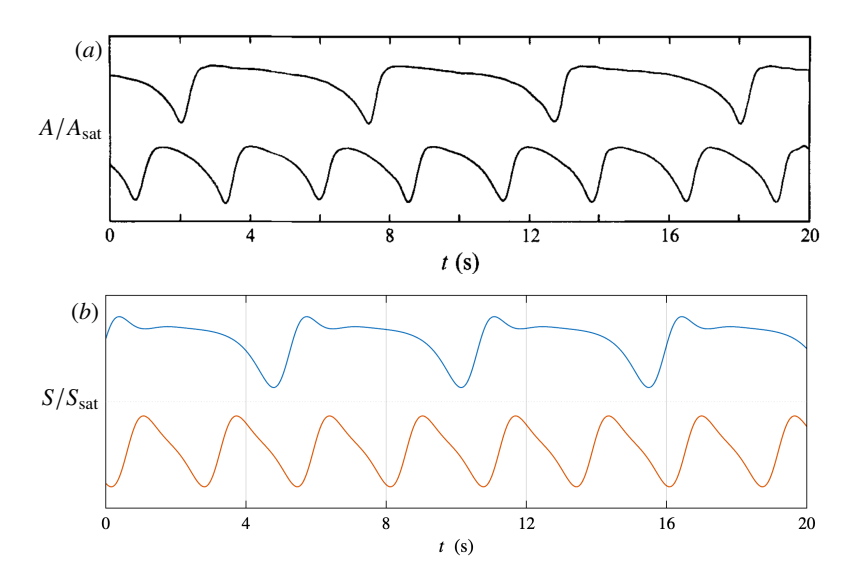


Figure 3: Evolution of the interfacial position: dominated by the fundamental and by the second harmonic. (a) Experimental traces (from Barthelet *et al.* (1995), p. 49); (b) Model computation.

computation always yields a slightly smaller  $T_{\rm sat}$ , which also appears in § 5.1. The pronounced asymmetry branch 2 wave observed here is a substantial improvement over the sine-like symmetric profile in figure 4(c) (Kalogirou *et al.* 2016). Unlike the saturation time shown in figure 4(b)(d) (Kalogirou *et al.* 2016), the saturation time to reach steady branch 2 is only around 1.5 times longer than which of branch 1.

#### 4.3. Basins of attraction

Here we focus on initial conditions in the region between branch 1 and branch 2, rather than on relatively large or small initial data. Define the initial conditions

$$H_0(\theta) = (1 - \theta) H_1 + \theta H_2, \quad \theta \in [0, 1],$$

where  $H_1$  represents (travelling wave solution) branch 1 and  $H_2$  represents branch 2. Given that we can always use  $H_0 = A\sin(x)$  to excite branch 1 and  $H_0 = A\sin(2x)$  for branch 2, the initial conditions can also be set as  $H_0(\theta) = (1-\theta)\sin(x) + \theta\sin(2x)$ . The basin of attraction of branch 1 is  $\mathcal{B}_1 = \left\{\theta \in [0,1] : \lim_{t\to\infty} \|H(\cdot,t;H_0(\theta)) - H_1\| = 0\right\}$ , and analogously for branch 2,  $\mathcal{B}_2 = \left\{\theta \in [0,1] : \lim_{t\to\infty} \|H(\cdot,t;H_0(\theta)) - H_2\| = 0\right\}$ . When both waves are stable, there exists a threshold  $\theta^* \in (0,1)$  such that  $\mathcal{B}_1 = [0,\theta^*)$  and  $\mathcal{B}_2 = (\theta^*,1]$ . The separatrix corresponds to  $\theta = \theta^*$ , i.e.  $\theta^* = \sup \mathcal{B}_1 = \inf \mathcal{B}_2$ .

In figure 4, for each  $\Lambda \in [0.0100, 0.0357]$  with step 0.001, the corresponding  $\theta^*$  (to three decimal places) is checked manually by the matching of the  $L^2$  norms of the travelling wave solutions (see figure 2(b)) and the  $L^2$  norms (from the dynamics) after a relatively long-time settlement. Branch 1 remains an attractor until  $\Lambda = 0.040$ , but its basin of attraction shrinks as  $\Lambda$  increases. Accordingly, the basin of branch 2 grows. However, once  $\Lambda$  reaches 0.0357, the basin of branch 2 collapses to zero: branch 2 becomes unstable and a new steady branch bifurcates from it and replaces it as the attractor. There is also a second bistability region  $\Lambda \in [0.0573, 0.0903]$  involving the new branch and branch 2. Since their  $L^2$  norms are very close in this interval, they are hard to distinguish by norms alone; one can still separate the

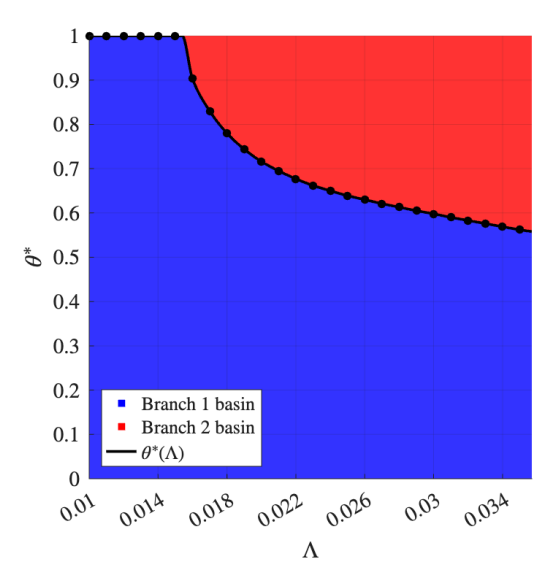


Figure 4: Basins of attraction for branch 1 and branch 2; bistability for  $\Lambda \in [0.0155, 0.0357]$ .

basins by inspecting wave profiles (the new branch is not a bimodal) or tracking the narrow gap of  $L^2$  norms.

## 5. Full comparison with the experiments Barthelet et al. (1995)

In this section, we present a full comparison between the experiment and the model of all the cases (d = 0.25), except for the bistability case, which is shown in § 4.2.

## 5.1. Interfacial profiles

For an overall comparison between the experiment (Barthelet *et al.* 1995) and the model, we examine the evolution of interfacial profiles and harmonic amplitudes near the onset of instability. All six cases were studied in detail by Barthelet *et al.* (1995). The interfacial shapes for  $U/U_L = \{1.33, 1.58, 1.77\}$  were shown in figure 3 of Kalogirou *et al.* (2016), but the evolution of harmonic amplitudes was not examined there.

 $U/U_L = \{1.06, 1.13, 1.33, 1.58, 1.77, 2.25\}$  corresponds to  $R = \{309.36, 329.78, 388.15, 461.11, 516.56, 656.65\}$ . The corresponding  $\Lambda = \{0.00449, 0.00479, 0.00564, 0.00669, 0.00750, 0.00953\}$ . We fix  $\Lambda = 0.00750$  at  $U/U_L = 1.77$ , where the model best matches the experimental interfacial shapes. For the same fluid,  $\Lambda \propto \text{Ca} \propto U$ ; we therefore scale  $\Lambda$  linearly with  $U/U_L$  to obtain the other values. Within the range explored here, variations in  $\Lambda$  produce only minor quantitative changes; the qualitative behaviour is governed primarily by R.

The agreement with experiment is excellent. The waves in both panels in figure 5 display similar profiles, with steep fronts and pronounced troughs that become more prominent as R increases, while the oscillation period shortens with increasing R. Similar as in § 4.2,  $T_{\rm sat}$  is scaled to 11.8, 11.1, 9.4, 8.1, 7.1, 6.5 respectively. The  $T_{\rm sat}$  calculated directly from the model is slightly smaller than the experiment. This shorter model  $T_{\rm sat}$  relative to experiment was also noted in table 3 (Kalogirou *et al.* 2016).

The bistability case can be seen as a continuation of the cases we study in this section, with a larger  $U/U_L$ . Although Barthelet *et al.* (1995) reported two distinct saturated waves only for

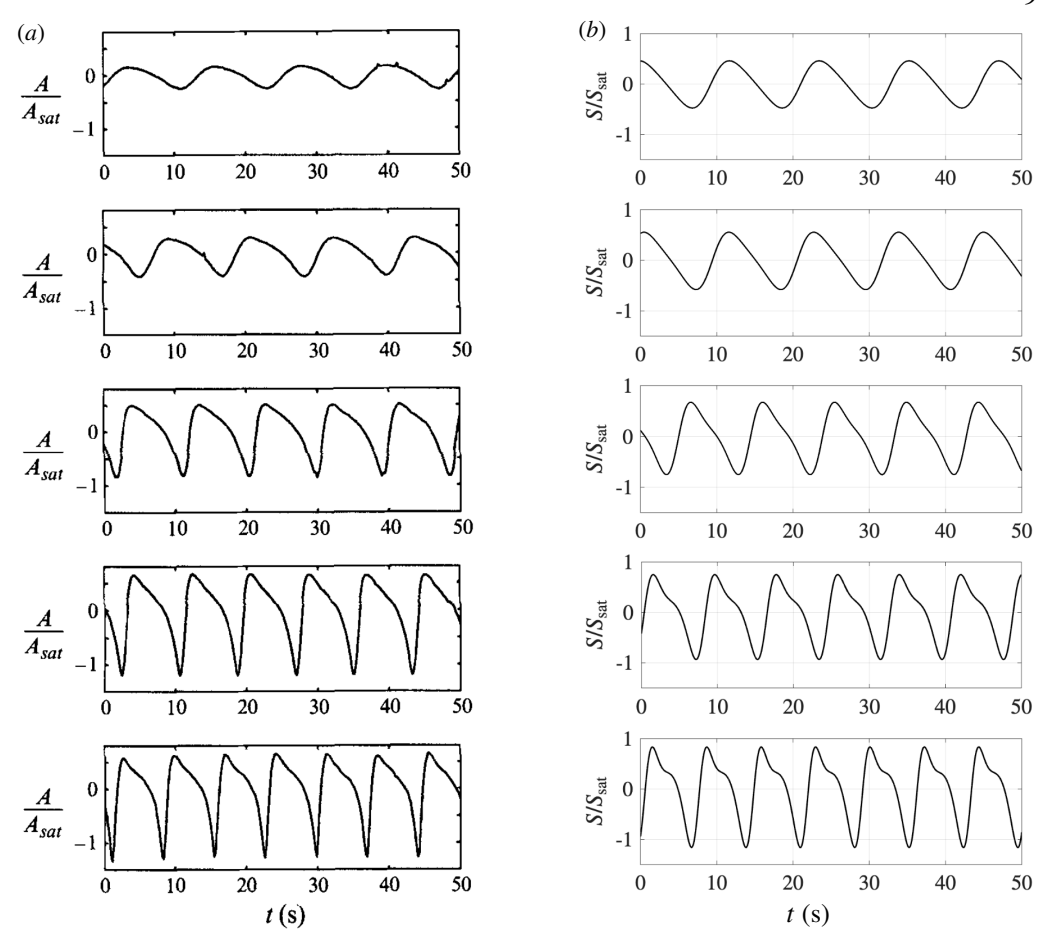


Figure 5: Interfacial profile for  $U/U_L = \{1.06, 1.13, 1.33, 1.58, 1.77\}$ .  $U_L = 0.138 \, \mathrm{m \, s^{-1}}$ . (a) Experimental shapes (from Barthelet *et al.* (1995), p.36); (b) Model computation. Amplitudes are normalised with the saturated amplitude for  $U/U_L = 1.77$ .

 $U > 2.4U_L$ , we find bistability (branch 1 and branch 2) also at  $U/U_L = 1.06, 1.58, 3.50$  (R = 309, 461, 1021), with corresponding bistability region  $\Lambda \in [0.023, 0.041]$ ,  $\Lambda \in [0.019, 0.042]$ , and  $\Lambda \in [0.014, 0.031]$ . For even larger R, the bistability window narrows.  $R \in [400, 800]$  provides a relatively wide window in which two distinct saturated waves are observable. Nevertheless, the basins of attraction vary with R, so it is plausible that some bistable regimes were not observed experimentally. The canonical scaling  $Ca = \varepsilon Ca_0$  may also add difficulty in translating the  $\Lambda$  back to the experiment.

#### 5.2. Harmonic amplitudes

In figure 6, the Reynolds number R increases from top to bottom. Larger R yields an earlier approach to saturation for every k. The experimental traces display small wiggles or brief dips during transients, which arise from random initial conditions in the laboratory and are not reproducible run to run. The evolution time (x axis) and the amplitude of harmonics (y axis) are different from the experiment up to a scaling. Despite these differences, the trends align closely: the ordering of appearance, the systematic reduction in time to plateau

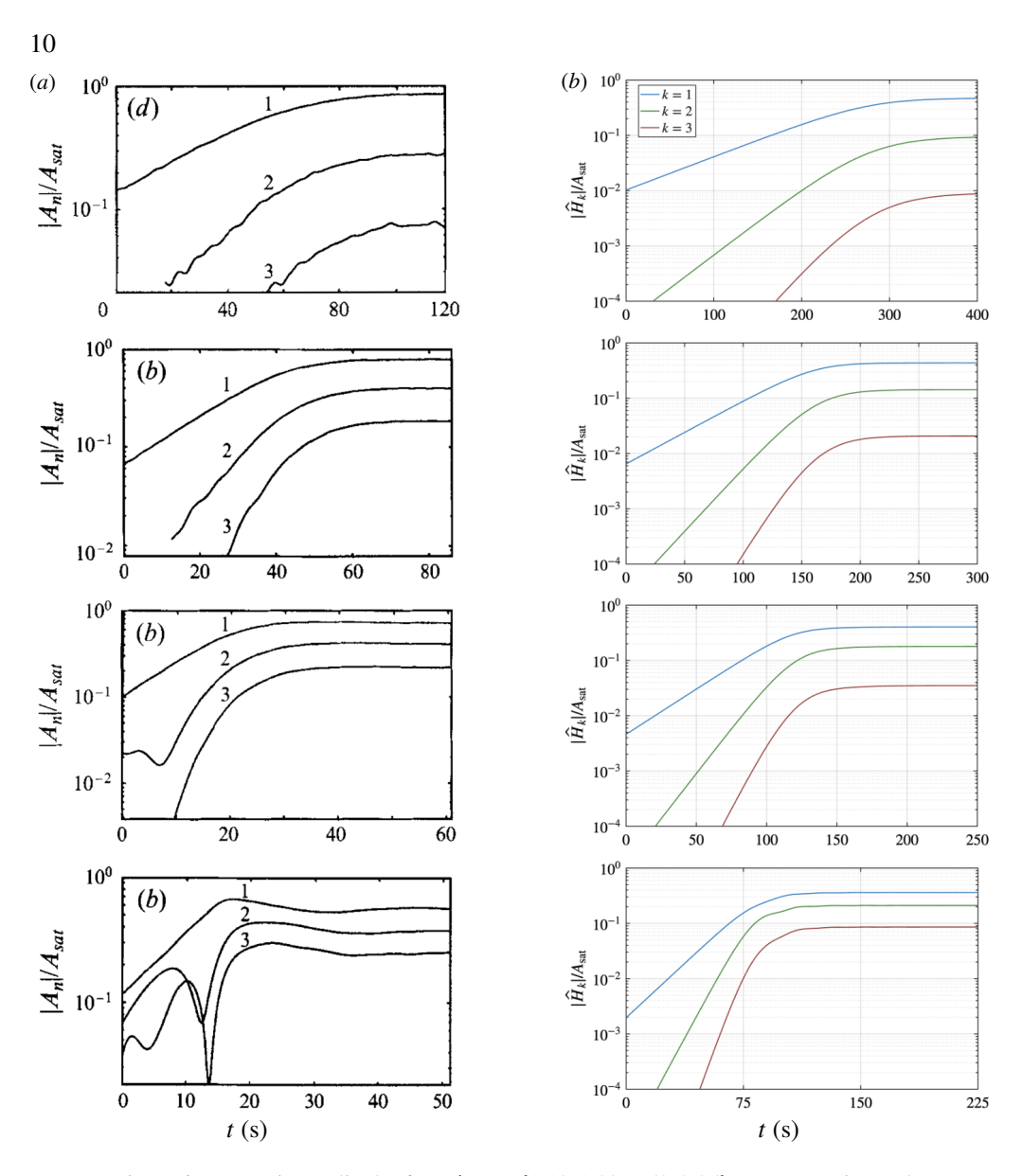


Figure 6: Harmonic amplitudes for  $U/U_L=\{1.13,1.33,1.58,2.25\}$ . (a) Experimental traces (from Barthelet *et al.* (1995), §§5.4 and 5.5); (b) Model computation.

with increasing R, and the progressive narrowing of the gap between the plateau levels of k = 1, 2, 3 as R increases. Again, the agreement with experiment is very good.

## 6. Discussion

The present study provides a comprehensive comparison between the model and the experiment (Barthelet *et al.* 1995) with all the examinable cases carefully checked. We perform a broad sweep over R and  $\Lambda$ , focusing on the bistability case; across these cases, we achieve sound agreement with experiment. It also turns out that the model performs very well

in fully capturing inertia in the thick layer through a linear nonlocal term which is coupled by the Orr–Sommerfeld problem.

If the experiment is reproduced in the future, it would be valuable to check carefully whether bistability appears at  $R \in [400, 800]$ . Indeed, according to the model, bistability may be more common than previously thought. A second focus of future research is the new branch observed here, which bifurcates from branch 2 at  $\Lambda = 0.0358$ . It will add clarity if one can prove the bifurcation type analytically. It would also be compelling to observe, in experiments, the bistability between branch 2 and this new branch for  $\Lambda \in [0.0573, 0.0904]$ .

#### REFERENCES

- Barthelet, P., Charru, F. & Fabre, J. 1995 Experimental study of interfacial long waves in a two-layer shear flow. *J. Fluid Mech.* **303**, 23–53.
- Charru, F. & Fabre, J. 1994 Long waves at the interface between two viscous fluids. *Phys. Fluids* 6 (3), 1223–1235.
- Craster, R. V. & Matar, O. K. 2009 Dynamics and stability of thin liquid films. *Rev. Mod. Phys.* 81, 1131–1198.
- HOOPER, A. P. 1985 Long-wave instability at the interface between two viscous fluids: thin-layer effects. *Phys. Fluids* **28**, 1613–1618.
- HOOPER, A. P. & BOYD, W. G. C. 1983 Shear-flow instability at the interface between two viscous fluids. *J. Fluid Mech.* **128**, 507–528.
- HOOPER, A. P. & GRIMSHAW, R. 1985 Nonlinear instability at the interface between two viscous fluids. *Phys. Fluids* **28**, 37–45.
- HOOPER, A. P. & GRIMSHAW, R. 1988 Travelling wave solutions to the kuramoto–sivashinsky equation. *Wave Motion* **10**, 405–420.
- Kalogirou, A. & Blyth, M. G. 2023 Nonlinear dynamics of unstably stratified two-layer shear flow in a horizontal channel. *J. Fluid Mech.* **955**, A32.
- Kalogirou, A., Cîmpeanu, R. & Blyth, M. G. 2020 Asymptotic modelling and direct numerical simulations of multilayer pressure-driven flows. *Eur. J. Mech. B/Fluids* **80**, 195–205.
- Kalogirou, A., Mpeanu, R. Cî, Keaveny, E. E. & Papageorgiou, D. T. 2016 Capturing nonlinear dynamics of two-fluid couette flows with asymptotic models. *J. Fluid Mech.* **806**, R1.
- Kalogirou, A. & Papageorgiou, D. T. 2016 Nonlinear dynamics of surfactant-laden two-fluid couette flows in the presence of inertia. *J. Fluid Mech.* **802**, 5–36.
- Katsiavria, A. & Papageorgiou, D. T. 2022 Nonlinear waves in viscous multilayer shear flows in the presence of interfacial slip. *Wave Motion* **114**, 103018.
- Katsiavria, A. & Papageorgiou, D. T. 2024 Stability analysis of viscous multi-layer shear flows with interfacial slip. *IMA J. Appl. Math.* **89** (2), 279–325.
- Монаммаді, А. & Smits, A. J. 2017 Linear stability of two-layer couette flows. *J. Fluid Mech.* **826**, 128–157.
- Mora Saenz, G. J. & Tanveer, S. 2024 Spectral stability of travelling waves in a thin-layer two-fluid Couette flow. *Proc. R. Soc. A* 480, 20230802.
- Papageorgiou, D. T. & Tanveer, S. 2019 Analysis and computations of a non-local thin-film model for two-fluid shear driven flows. *Proc. R. Soc. A* **475** (2230), 20190367.
- Papageorgiou, D. T. & Tanveer, S. 2021 Mathematical study of a system of multi-dimensional non-local evolution equations describing surfactant-laden two-fluid shear flows. *Proc. R. Soc. A* 477, 20210307.
- Papageorgiou, D. T. & Tanveer, S. 2023 Singular effect of interfacial slip for an otherwise stable two-layer shear flow: analysis and computations. *Proc. R. Soc. A* **479** (2272), 20220720.
- Ray, P. K., Hauge, J. & Papageorgiou, D. T. 2018 Nonlinear interfacial instability in two-fluid viscoelastic Couette flow. *J. Non-Newtonian Fluid Mech.* **251**, 17–32.
- Renardy, Y. Y. 1985 Instability at the interface between two shearing fluids in a channel. *Phys. Fluids* **28**, 3441–3443.
- Renardy, Y. Y. 1987 The thin-layer effect and interfacial stability in a two-layer couette flow with similar liquids. *Phys. Fluids* **30**, 1627–1637.
- YIH, C.-S. 1967 Instability due to viscosity stratification. J. Fluid Mech. 27, 337–352.